Anisotropic Behavior of Optical Properties in Edge-Modified Phosphorene Quantum Dots

W.M. Uvin G. De Alwis and Kevin L. Shuford*

Department of Chemistry and Biochemistry, Baylor University, One Bear Place #97348, Waco, TX 76798-7348, USA

* Kevin_Shuford@baylor.edu, 1-254-710-2576, fax : 1-254-710-4272

Abstract

The evolution of optical properties in low dimensional phosphorene quantum dots remains a largely unexplored area, with great potential for applications as optoelectronic devices. Herein, we present a comprehensive analysis of the optical properties of edge-passivated (H, NH_2, Cl, OCN, CN) monolayer phosphorene quantum dots using Density Functional Theory and Time-Dependent Density Functional Theory calculations. An extensive characterization of absorptions, non-radiative relaxations, radiative emissions, radiative lifetimes, and the high-frequency Raman modes (A_g^1 , B_{2g}, and A_g^2) is undertaken, emphasizing the role of material directionality, quantum confinement, and edge passivation on the evolution of these properties. Our results indicate that optical absorptions and emissions are preferred from the armchair direction of phosphorene regardless of the type of edge-functionalization or system size, rendering these systems as potential natural linear optical polarizers in the UV-Vis region. Larger phosphorene quantum dots have smaller Stokes shifts and less geometric variation upon relaxation, leading to decreased radiative lifetimes. Additionally, we identify an uncharacteristic Raman response associated with dissimilar shifting trends of the A_g peaks that arise from planar growth of phosphorene quantum dots in the armchair or the zigzag direction. The behavior is attributed to the competing effects of mass coupling and improved bond strength.

1. Introduction

Phosphorene is a recent addition to the 2D material family that has emerged since the discovery of graphene.[1, 2] It began to receive significant attention upon the successful fabrication of a field-effect transistor constructed using exfoliated black phosphorous (BP).[3, 4] The quest for high performance nanoscale devices has resulted in a flurry of research activity utilizing phosphorene for a wide variety of applications including optoelectronics,[5-7] sensing,[8-10] energy storage,[11, 12] thermoelectrics,[13-15] photovoltaics,[16] spintronics,[17, 18] and biomedicine.[19-21] Further efforts have focused on generation of phosphorene using top-down methods, such as mechanical and liquid exfoliation,[22-24] or bottom-up methods like chemical vapor deposition[25, 26] and epitaxial growth.[27, 28] The impetus for incorporating phosphorene (and derivatives) into device applications can be attributed to its favorable, highly tunable, and anisotropic physical (electronic band structure, electric and thermal transport, optical)[3, 14, 29-31] and mechanical (Young's modulus, Poisson's ratio, critical strain) properties.[32-34]

Phosphorene's novel properties are fundamentally rooted in the unique structure of BP, a stable allotrope of phosphorous. BP crystals consist of puckered honeycomb layers of phosphorene adhered via weak van der Waals interactions, which enables exfoliation of 2D sheets from the bulk crystal. A phosphorene sheet consists of phosphorous atoms (P) bonded to three other neighboring P atoms that adopt an sp^3 hybridization scheme. This arrangement promotes the inherent anisotropy of the material, resulting in two distinct directions commonly known as the armchair (puckered structure) and zigzag directions (bilayer structure). Angle-resolved polarized Raman spectroscopy has been utilized as a non-destructive way of identifying the BP crystal orientation (armchair and zigzag direction) based on the intensity variation of the A_g^2 mode as a function of the sample rotation angle.[35] This structural anisotropy is also reflected in its bonding scheme where

the shorter bond length (~ 2.224 Å) connects the nearest P atoms within a single plane, while the longer bond length (~ 2.244 Å) connects the nearest P atoms in two planes. A similar change is observed for the in-plane (~ 96.3^0) and out-of-plane (~ 102.3^0) bonding angles between these P atoms.[36, 37]

Previous studies have shown the intrinsic anisotropy is manifested in the optical properties of direct excitons of phosphorene, as well as indirect excitons residing in heterostructures of phosphorene, through enhanced absorption and higher exciton binding energies along the armchair direction.[38, 39] Furthermore, this inherent anisotropy of phosphorene has resulted in certain heterostructures of phosphorene achieving anisotropic superfluidity, thereby garnering attention as promising candidates for Bose-Einstein condensation and superfluidity at high temperatures.[38, 40, 41] Photons with polarization parallel to the zigzag direction of phosphorene have been shown to excite lower valence band electrons to the upper conduction bands under certain conditions, generally requiring a frequency deeper into the ultraviolet regime.[39, 42] The optical properties of more confined 1D nanoribbons of phosphorene also display the anisotropic nature of these systems. Zigzag and armchair nanoribbons have been reported to have different band gap scaling laws resulting from the dissimilar electron and hole behavior along these directions.[43] Density Functional Theory (DFT) calculations using PBE and HSE06 predict that pristine armchair nanoribbons are indirect band gap semiconductors.[44] However when passivated at the edges, these armchair nanoribbons transform into direct band gap semiconductors. As a result, the first peak in the absorption spectra is optically active, corresponding to transitions from the valence band to conduction band, as opposed to zigzag nanoribbons that are known to have dark symmetry gaps with active higher energy transitions.[43, 44] Preferential absorption of light polarized along the armchair direction has been reported in certain phosphorene quantum dots using tight-binding

methods.[45-47] These quantum dot systems typically possess fundamental band gaps and optical gaps that are largely governed by quantum confinement. Emission gaps for certain PQDs have been shown to have more complex trends due to competing relaxation effects.[48]

Fundamental knowledge regarding the optical and electronic properties of 0D phosphorene quantum dots (PQDs) is still in its infancy when compared to the 2D and 1D counterparts. Reducing size produces PQDs with discretized energy levels and may also provide enhanced functionality via ease of chemical modification and improved stability.[49] Some existing examples in the literature include PQD systems being used for multilevel data storage,[50] electrocatalysts for the oxygen evolution reaction,[51] and bioimaging/cancer therapy.[52] Obtaining a deeper understanding of how PQD properties evolve with system size and varied surface chemistry is of high importance for these systems to be utilized in future device applications. Herein we present a comprehensive characterization of vertical excitations (absorption), non-radiative relaxation, vertical de-excitation (emission), and radiative lifetimes of PQDs by varying material anisotropy, PQD size, and chemical composition of edge terminations. We examine the nature of the charge carriers (electrons and holes) generated upon excitation and present quantifiable parameters for the structural rearrangement that occurs due to non-radiative relaxation. The Strickler-Berg relationship is utilized to calculate radiative relaxation lifetimes and elucidate the emission properties of the hydrogen functionalized PQDs. Lastly, the Raman response of PQDs is discussed with respect to material anisotropy, PQD size, and edge termination.

2. Computational Details

This study investigates monolayer PQDs with a diameter ranging from 1.6 - 3.6 nm inclusive of edge functional groups. The diameter is defined as the distance between the boundary atoms of a

given PQD that are furthest apart along with their van der Waals radii[53] determined with the aid of Multiwfn 3.8[54] (see Table S1 in the Supporting Information for PQD size information). This size regime was chosen to capture the effects of quantum confinement and material anisotropy on the PQD optical properties. Edge sites, the number of which are denoted on the axes of Figure 1, correspond to functionalization locations for a given quantum dot. This numeric value is also used as a metric to indicate the system size along a particular direction. In most cases, edge functionalization with H atoms was used to terminate the PQDs and avoid dangling bonds. Dangling bonds here refer to the exterior P atoms that are only connected to two other neighboring P atoms resulting in an unsatisfied valency. NH_2, Cl, OCN, and CN groups were also investigated as PQD terminations to gauge the effects of different functional groups on the optical properties of these systems (see Figure S1 for depiction of functionalized PQDs). This termination scheme was used in our

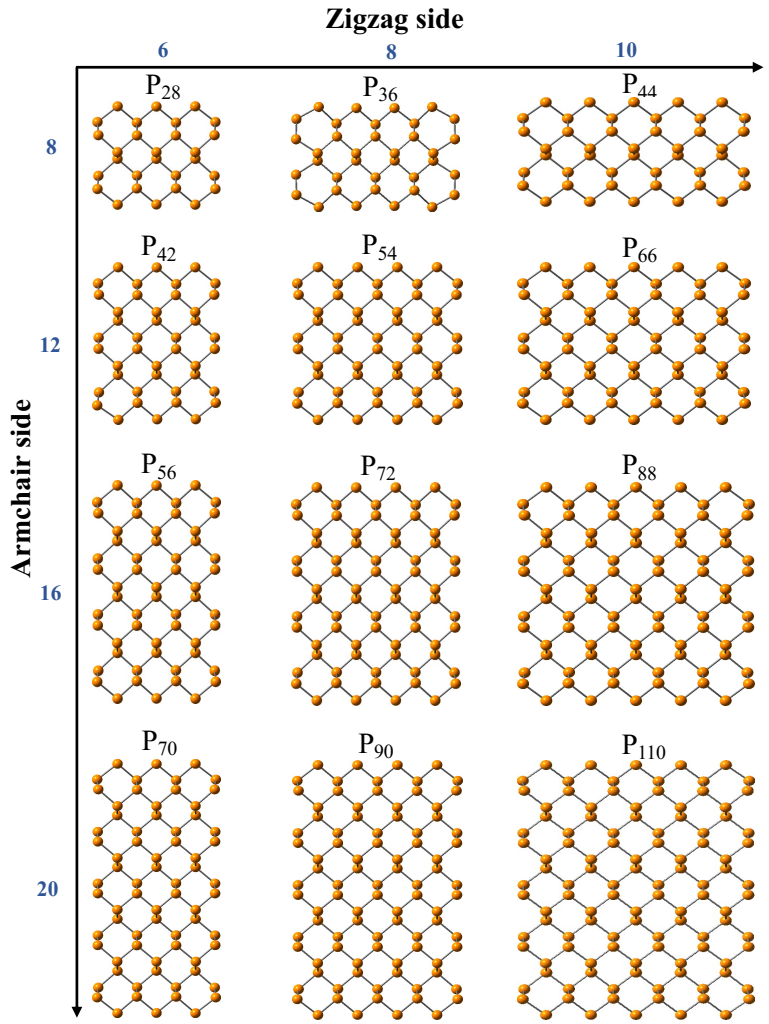

Figure 1: Top view of the PQDs. Passivation at the edges is removed for clarity. Orange spheres denote phosphorus atoms.

previous work and found to alter the electrostatic potential landscape by creating edge dipole layers that effectively shift the energetics of all orbitals.[55]

Full geometry optimizations were performed on the ground state structures (S_0) of the PQDs using the Becke 3-parameter Lee-Yang-Parr (B3LYP)[56-58] global hybrid density functional in conjunction with a Pople-type split valence, triple-ζ basis set (i.e., 6-311g (d,p)) with polarization functions (d orbitals on non-hydrogen atoms and p on hydrogen atoms). All computations were performed using a pruned grid (99 radial shells, 590 angular points per shell) along with a threshold of $< 10^{-10}$ for the RMS change in the density matrix during the self-consistent field procedure. Harmonic vibrational frequencies were calculated to ensure that the structures correspond to a minimum on the B3LYP potential energy surface. Raman activities were obtained, and spectral features were generated using a Lorentzian function with a full width at half max of 6 cm^{-1}.

Time-dependent density functional theory[59-62] (TD-DFT) single point energy computations were performed at the same level of theory to identify the first 200 singlet excited states. These were used to identify the optical energy gap (E_{opt}), defined as the energy of the first optically active excitation, and the corresponding wavelength (λ_{opt}). Triplet excitations have not been considered in this work, as it has been shown that electron-hole pair generation primarily occurs from the singlet state for similar quantum dots.[48] Simulated absorption spectra were generated using a full width at half max of 0.1 eV, while the directional responses were plotted by taking the specific contribution of the transition dipole moment with the aid of Multiwfn 3.8. Further analysis on the E_{opt} transition was performed to obtain the electronic transition dipole moment, oscillator strength, electron density, hole density, and overlap between electron and hole density distributions (S_r

index) using Multiwfn.[54] The applicability of these descriptors to confined nanoclusters can be found in the literature.[63]

Gradient calculations were performed on the excited state corresponding to E_{opt} at the same level of theory as the ground state structure optimizations for the hydrogen-terminated PQDs. These calculations were utilized to determine radiative emission energy (E_{emi}), Stokes shift (E_{opt} - E_{emi}), radiative lifetime, and the electron-hole overlap (S_r index) corresponding to the emission. Arbalign,[64] a standalone python script that utilizes the Kuhn-Munkres structure matching algorithm,[65, 66] was employed to calculate the lowest RMSD between the ground state optimized structure (S_0) and the corresponding excited state optimized structure (S_n) of a given PQD. This procedure was used to quantify the structural change that occurs during the excited state relaxation process.

All electronic structure computations were performed using the Gaussian 16 software suite.[67] Kohn-Sham orbital figures of the HOMO and LUMO were constructed via projection onto a total electron density iso-surface at 0.02 a.u., while electron and hole regions were constructed with a projection onto a total electron density iso-surface at 0.0007 a.u. These images were generated using Tachyon ray tracing libraries[68] available in the Visual Molecular Dynamics software.[69]

3. Results and Discussion

First, we examine the role of structural anisotropy on Frank Condon excitations (vertical excitations). Figure 2 depicts the simulated absorption spectra of hydrogen functionalized PQDs along with the contribution to absorption arising specifically from the electric field oscillating in the armchair direction. It is evident that PQDs with shorter armchair lengths (top row of Fig. 2)

display a notable optical response along the zigzag direction in the UV range. These higher-energy absorption features converge to the armchair contributions moving from the top row down each column. The analogous TD-DFT calculations with the range-separated global hybrid CAM-B3LYP functional[70] (see Supporting Information, Fig. S2) show the UV excitations are further enhanced from the electric field oscillating in the zigzag direction even for the larger PQDs, which suggests the high energy features are long-range in nature. In the low energy regions where armchair contributions dominate, the CAM-B3LYP results are consistent with the trends in Figure 2 (barring systematic blue shifts and increased optical activity, Fig. S3). Thus, for our purposes here, B3LYP is deemed sufficient to describe the low energy excitations that correspond to the optical gap, which are typically short range in nature for these PQDs. Note, the excitations associated with E_{opt} are almost exclusively HOMO to LUMO transitions (> 93% on average; Table S1) and are the global absorption maximum for majority of the systems under

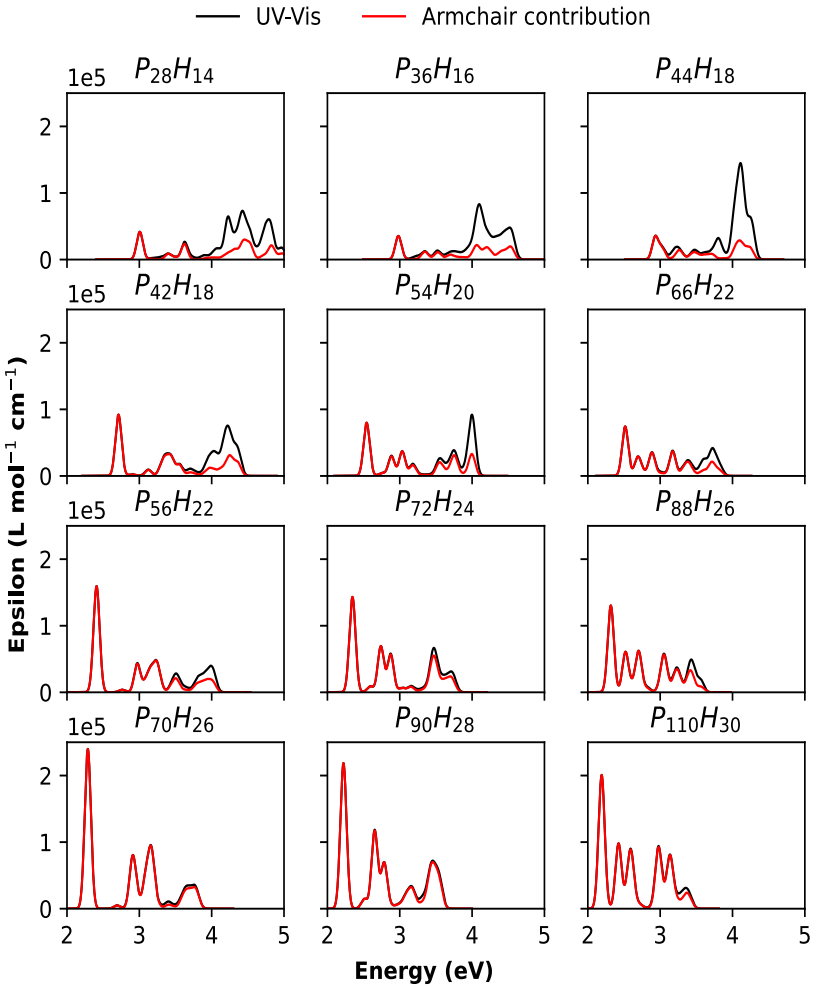

Figure 2: Simulated absorption spectra for H terminated PQDs.

Table 1: Properties of hydrogen functionalized PQDs. Electronic fundamental gaps (E_{gap}), optical gaps (E_{opt}), and excitation properties at λ_{opt}. S_r Index is the e-h overlap upon absorption.

System	E_{gap} (eV)	E_{opt} (eV)	Transition dipole moment (a.u.)			Oscillator strength	S_r Index (a.u)
			Armchair	Zigzag	Out of plane		
$P_{28}H_{14}$	3.51	3.01	1.448	0.000	-0.057	0.155	0.715
$P_{42}H_{18}$	3.16	2.71	2.266	-0.010	-0.034	0.341	0.726
$P_{56}H_{22}$	2.82	2.41	-3.167	0.000	-0.027	0.592	0.738
$P_{70}H_{26}$	2.68	2.29	3.984	0.000	0.023	0.890	0.738
$P_{36}H_{16}$	3.49	2.98	1.336	0.022	-0.062	0.131	0.690
$P_{54}H_{20}$	2.97	2.54	-2.181	0.000	0.003	0.296	0.731
$P_{72}H_{24}$	2.74	2.35	3.040	0.000	0.027	0.531	0.739
$P_{90}H_{28}$	2.60	2.22	3.860	0.000	0.022	0.811	0.740
$P_{44}H_{18}$	3.41	2.93	-1.324	0.000	-0.054	0.126	0.698
$P_{66}H_{22}$	2.93	2.52	-2.115	0.000	0.030	0.276	0.727
$P_{88}H_{26}$	2.70	2.32	-2.918	0.000	-0.028	0.484	0.739
$P_{110}H_{30}$	2.55	2.19	-3.726	0.000	0.024	0.745	0.741

study. The oscillator strength values in Table 1 and the first peak in all panels of Figure 2 suggest that increasing quantum dot size along the zigzag direction while holding the armchair edges constant (moving right across a row in Fig. 2) results in a subtle red shift and a slight reduction in the intensity of the E_{opt} peak. Furthermore, increasing system size in the armchair direction while holding zigzag edge constant (moving down a column) results in red shifts and notable increases in the intensity of the E_{opt} peak. Slight variations in the red-shifting behavior upon anisotropic growth can be attributed to the dissimilar behavior of electrons in the two directions.[43] Generally, the intensity of a transition will depend on the overlap between the initial and final states of the wave function and selection rules that are determined by symmetry. The consistent S_r index values in Table 1 suggest that the overlap between initial and final states is not a driving factor for the dissimilar trends in peak intensity. Thus, it can be attributed to the forbidden nature of transitions along the zigzag direction, which is also reflected by the corresponding transition dipole moment values. This indicates that these phosphorene quantum dots behave analogously to the extended

2D material and thus can be utilized as natural optical linear polarizers due to preferential absorption along the armchair direction.

We next present the effects introduced upon altering the PQD termination with different chemical groups. Figure 3 depicts UV-Vis spectra for all PQDs considering the first 10 singlet excitations for clarity, as this encapsulates the low energy HOMO-LUMO transitions of interest for the PQDs. Quantum confinement effects are observed through red shifts in the E_{opt} transition of all spectra with increasing system size in either direction (Figure 3 and Table S1). The red shifts along the armchair direction are more pronounced and can be attributed to a similar trend in the fundamental gap ($\Delta E_{|HOMO-LUMO|}$) behavior that has been discussed in previous work.[55] A wider distribution of the E_{opt} transition energies for

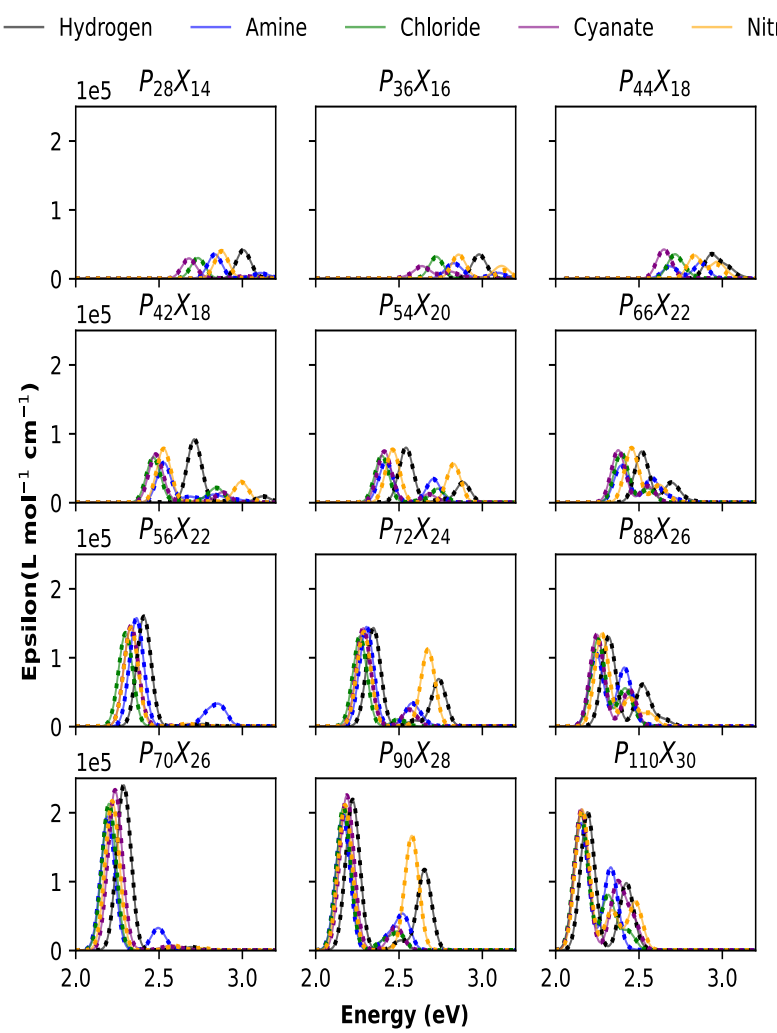

Figure 3: Truncated absorption spectra consisting of the 10 lowest lying excitations of PQDs where X = H, NH_2, Cl, OCN, CN. The dotted curves indicate the response from light oscillating in the armchair direction of the PQDs, while the solid curve indicates the response from unpolarized light.

different terminations can be observed for the smaller PQDs in Figure 3, while these features coincide for the larger PQDs. Since these optical features are primarily governed by HOMO – LUMO transitions (Table S1), they follow a similar trend to the fundamental gaps of these PQDs. In general, the edge groups have low contributions to the HOMO and LUMO orbitals of the smaller PQDs, while as PQD size is increased the contribution from these edge states to the frontier orbitals become nonexistent (see Figure S4 and our previous work[55]). As a result, the fundamental gaps, and by extension optical gaps, of larger PQDs are resistant to change despite the different edge terminations. The dotted curves in Figure 3, which denote the armchair response of the UV-Vis spectrum, coincide with the overall response, indicating the chemical groups used for termination do not play any role in determining the selection rules for these transitions. Thus, the ability of these PQDs to function as linear optical polarizers is preserved despite modifications to the chemical identity of edge groups.

Next, we examine relaxation of excitons generated from the E_{opt} absorption for hydrogen terminated PQDs. Radiative relaxation (E_{emi}) is often preceded by a vibrational relaxation from a vibrationally excited state to the vibrational ground state of the electronically excited potential energy surface. The Stokes shift, which is defined as the energy difference between E_{opt} absorption and the corresponding emission energy E_{emi}, can be utilized as a metric to gauge the extent of non-radiative relaxation. Non-radiative relaxation is accompanied by a change in geometry of the quantum dots. The extent of change in the geometric structure is reported as RMSD values in Table 2, where the RMSD is calculated with respect to the optimized ground state structure. A general reduction in Stokes shift is observed when system size is increased along either the armchair direction or zigzag direction. A smaller Stokes shift indicates a smaller energy change for non-radiative relaxation, which typically indicates that the corresponding geometric change is also

Table 2: Radiative and non-radiative relaxation properties for hydrogen functionalized PQDs excited at λ_{opt}. S_r Index is the e-h overlap for emission, ΔS_r is the change in S_r Index from absorption to emission, and RMSD is the structural change of relaxation.

System	E_{opt} (eV)	E_{emi} (eV)	Stokes Shift (eV)	Radiative lifetime (ns)	S_r Index (a.u.)	ΔS_r	RMSD (Å)	Transition dipole moment (a.u.)			Oscillator strength
								Armchair	Zigzag	Out of plane	
$P_{28}H_{14}$	3.01	1.60	1.41	348.4	0.578	0.137	0.405	-0.812	0.000	0.000	0.026
$P_{42}H_{18}$	2.71	1.67	1.04	42.2	0.702	0.024	0.170	2.190	-0.010	-0.086	0.196
$P_{56}H_{22}$	2.41	2.03	0.38	10.3	0.713	0.025	0.105	-3.300	0.000	-0.002	0.541
$P_{70}H_{26}$	2.29	1.99	0.30	6.8	0.715	0.023	0.071	4.182	0.000	0.008	0.852
$P_{36}H_{16}$	2.98	1.60	1.38	437.5	0.576	0.114	0.358	0.723	-0.026	0.041	0.021
$P_{54}H_{20}$	2.54	1.63	0.91	54.1	0.707	0.024	0.135	-1.998	0.000	0.089	0.160
$P_{72}H_{24}$	2.35	2.02	0.33	12.2	0.703	0.036	0.068	3.059	0.000	0.022	0.463
$P_{90}H_{28}$	2.22	1.96	0.26	8.1	0.703	0.037	0.056	3.918	0.000	0.017	0.737
$P_{44}H_{18}$	2.93	1.95	0.98	212.4	0.429	0.269	0.112	-0.817	0.000	0.023	0.032
$P_{66}H_{22}$	2.52	1.98	0.53	33.8	0.671	0.056	0.138	-1.888	0.000	0.013	0.173
$P_{88}H_{26}$	2.32	2.01	0.31	14.5	0.684	0.055	0.085	-2.822	0.000	-0.013	0.393
$P_{110}H_{30}$	2.19	1.95	0.24	9.3	0.691	0.050	0.047	-3.676	0.000	0.015	0.647

small. This is observed by the relatively smaller RMSD values seen for the larger quantum dot sizes in Table 2, particularly when increasing size along the armchair direction. Thus, increasing PQD size along armchair direction results in these PQDs obtaining structural rigidity against external perturbations in electron density due to absorptions and emissions. Non-radiative transitions generally follow the "energy gap law", and hence when the energy gap is higher, the non-radiative rate of transfer (k_{nrad}) from initial to final states is lower ($k_{nrad} \sim e^{-\Delta E}$).[71, 72] The smaller PQDs, which display higher stokes shift according to the energy gap law, would typically have a lower population transfer rate to the ground vibrational state of the electronically excited potential energy surface. This lower population transfer rate for smaller PQDs is expected considering the degree of structural change observed for these systems. The effect of the structural changes on the electronic structure of these quantum dots is reflected by the frontier orbital iso-surface maps and the electron hole densities in Figure 4 as well as the frontier orbital energy diagrams (Figure S5). Smaller PQDs display a large electron density shift and energy shift in the HOMO and LUMO orbitals due to non-radiative relaxation. Similarly, a visual change in electron and hole distributions of the smaller quantum dot size can be seen in Figure 4. This results in a reduction in the overlap region between initial and final states of the emission process for smaller

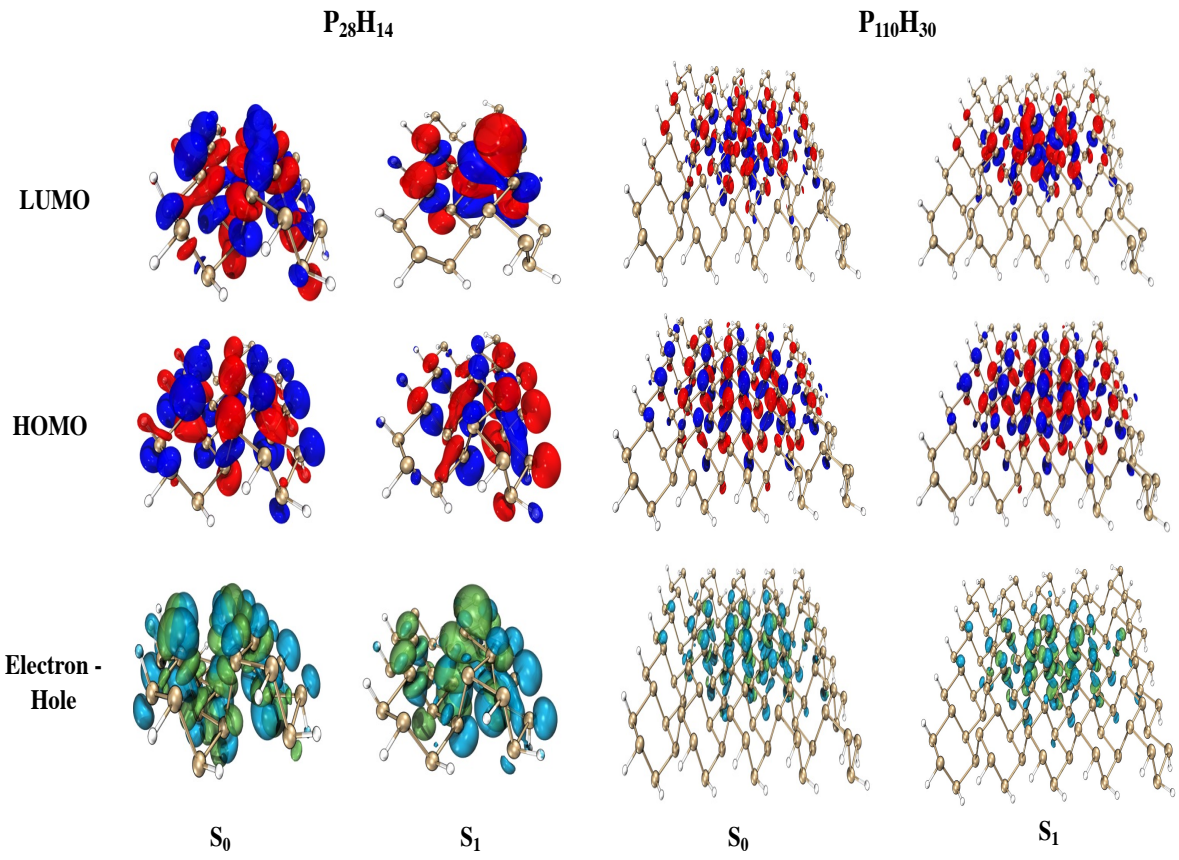

Figure 4: HOMO, LUMO orbital iso-surfaces (red indicates negative and blue indicates positive phases) and electron hole densities (green indicates electron and blue indicates hole region) for ground state (S_0) and excited state (S_1) of smallest and largest PQDs.

PQDs (see S_r index for the excited surface and ΔS_r indices in Table 2). These effects are muted for the larger PQDs, where the iso-surfaces are more similar and geometric variations are less noticeable.

Now we focus on the radiative decay that takes place following relaxation to the ground vibrational state of the excited potential energy surface. The radiative decay follows the Frank Condon principal to a final state in the ground electronic potential energy surface. The final state would most often be a vibrationally excited state in the ground electronic potential energy surface that has good wave function overlap with the initial state. The lifetime for this radiative decay has been calculated using a form of the Strickler Berg relationship: $\boldsymbol{k_i} = \frac{\mathbf{1}}{\boldsymbol{\tau_i}} =$

$\frac{4}{3t_0}\alpha_0^3(\Delta E_i)^3\sum_{\alpha\epsilon\{x,y,z\}}\left|M_\alpha^i\right|^2$, where k_i is the radiative rate, τ_i is the radiative lifetime, ΔE_i is the corresponding energy attributed to the particular radiative emission, M_α^i is the transition dipole moment, $t_0 = {\{4\pi\varepsilon_0\}^2\hbar^3}/{m_e e^4}$ and α_0 is the fine structure constant.[73-75] The radiative decay lifetime of these excitons displays an exponential decrease when PQD size is increased along the armchair direction while holding zigzag direction constant (Table 2). This can be attributed to the general blue shifting trend in emission energy and the increasing trend in the magnitude of transition dipole moment along the armchair direction. This gives rise to two important observations regarding PQD emissions. The first is that radiative emission, like absorption, also preferentially occurs from the armchair side as indicated by the transition dipole moments in Table 2. An important point to note here is that emissions are less intense than the corresponding absorption. This observation can be tied to the geometric change during non-radiative relaxation that results in a change in electronic structure. This is reflected in the corresponding ΔS_r index values, which is quite significant for the smaller PQDs (Table 2). As a result of the lower overlap between the initial and final states, these PQDs display smaller intensities for emission than absorption. However, increasing PQD size, particularly in the armchair direction, increases the intensity of the emission in a similar fashion to absorption. The second observation is that while PQDs have a general blue shifting trend in emission with size, the largest structure for a given zigzag configuration shows a red shift in energy with increasing armchair dimension (deviations exist for zigzag extension too but are more muted). Anomalous behavior of emissions has been reported previously in PQDs.[48] This can be attributed to the competing quantum confinement and relaxation effects, as observed here. Beyond a particular size, the quantum confinement effects predominate giving rise to the observed red shift.

Lastly, we present the Raman spectra of the hydrogen functionalized PQDs. The spectra shown in Figure 5 are truncated to display the high-frequency region where the commonly discussed Raman active modes of pristine phosphorene reside. Thus, it does not capture the Raman signals pertaining to the uncoupled vibrations of the hydrogen atoms. Generally, the lowest energy peak, which is the A_g^1 mode, corresponds to vibrations that are perpendicular to both the armchair and zigzag directions of phosphorene (out-of-plane vibrations). The next peak is the B_{2g} mode that corresponds to vibrations along the zigzag direction, while the final peak is the A_g^2 mode that corresponds to vibrations along the armchair direction.[76] These characteristic high-frequency Raman modes for bulk BP are known to be around 365 cm^{-1}, 440 cm^{-1}, and 470 cm^{-1} respectively.[77]

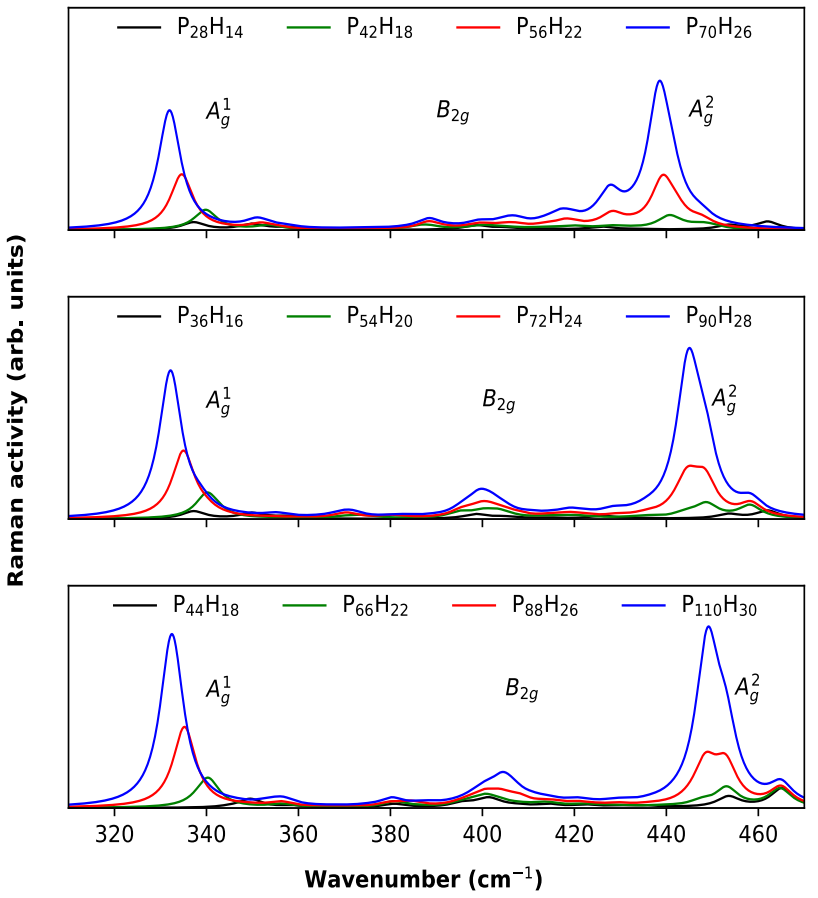

Figure 5: Truncated Raman spectra depicting the high-frequency Raman modes for hydrogen functionalized PQDs.

Previous reports indicate the high-frequency modes are affected by the number of layers of pristine phosphorene.[78-80] The A_g^1 mode is the most sensitive to the layer thickness out of the high-frequency modes, resulting in a significant increase in activity in comparison to the A_g^2 mode with increasing number of layers.[79] The heightened

sensitivity of the A_g^1 mode to layer thickness is not relevant here, as this study pertains to the planar growth of PQDs (i.e., an increase along armchair or zigzag directions). Increasing system size along the armchair direction (i.e., systems within a single panel of Figure 5) induces a significant increase in activities for both of the A_g modes, which can be attributed to the enhanced polarizabilities. This effect is further accentuated for the A_g^2 mode due to the vibrations being along the armchair direction. An increase in activity for the B_{2g} mode can also be observed; however, this mode is less sensitive to the increase in system size along armchair direction. Planar growth along the armchair direction results in a noticeable red shift in the A_g peaks. Increasing PQD size along the zigzag direction (same color curves in different panels of Figure 5) corresponds to a slight increase in Raman activity and a noticeable blue shift in the B_{2g} and A_g^2 peaks. It is worth noting that the edge terminations employed in this study initiate new vibrations that are also active at these frequencies complicating the analysis. Furthermore, these high-frequency peaks (A_g^1, B_{2g}, A_g^2) consist of multiple contributions from similar vibrations that are separated spatially within the PQD and local in nature (see Figure S6). These artifacts are more prominent in the weaker B_{2g} mode convoluting its analysis, so we will mainly focus on the more conspicuous A_g modes. The trends in the A_g peak shifts can be ascribed to the competition between mass coupling effects and bond strength variations with system size, as illustrated by the force constants and reduced masses for a particular Raman mode (Table S2). The red shifting behavior of the A_g^1 and A_g^2 peaks when the system size is increased along the armchair direction can be attributed to the higher degree of mass coupling, which is more dominant than the increase in bonding strength (see ratios of force constant and reduced mass in Table S2), while the blue shifting behavior observed for the A_g^2 peaks when PQD size is increased in zigzag direction can be attributed to the increase in force constants over the mass coupling (Table S2). This indicates that the anisotropic growth of

these PQDs provides significant control over the peak shifting behavior. The Raman spectra for PQDs with the different edge terminations remain largely unaltered in comparison to the hydrogen terminations (see Figure S7). Notable exceptions are increased activities of the high-frequency modes for edge terminations like cyanate (OCN) groups, which have the largest PQD diameters (Table S1) resulting in larger surface areas that are polarizable, and shifts in peak positions for nitrile edge terminations, which arise from changes to bond strengths resulting from the electron density redistribution from edge functionalization.

4. **Conclusions**

In summary, this study focuses on the role of material anisotropy, chemical identity of edge terminations, and quantum confinement on the optical properties of edge modified monolayer phosphorene quantum dots. Our results indicate that all PQDs in this size regime (approx. 1.6-3.6 nm in diameter) behave as natural linear optical polarizers by preferentially absorbing and emitting light primarily from the armchair direction. This holds true despite the chemical identity of the edge passivating groups, as these functionalizations do not contribute significantly to the orbitals associated with the excitations being considered. The observed preferential absorption from the armchair direction in the low energy regime occurs regardless of the length ratio between armchair and zigzag edges; although, optical responses in the high energy range from electric fields oscillating in the zigzag direction can be observed when the armchair to zigzag length ratio is lowered. The nonexistent optical activity in the lower energy range from the zigzag direction can be attributed to symmetry restrictions, which is also observed in extended systems of phosphorene. Furthermore, the intensity of the optical absorption and emission signals can be increased by increasing system size along armchair direction. Thus, quantum confinement effects do play a

secondary role in tuning the intensity of the absorption and emission responses. Quantum confinement effects also contribute to the non-radiative relaxation and radiative decay lifetimes for the photogenerated excitons. This information can be useful for applications that utilize phosphorene-based composite materials as luminescent devices. Distinct differentiation of the three high frequency Raman modes of bulk BP can be made for monolayer PQDs of considerable diameter (roughly greater than 2 nm here). In general, the A_g^1 and A_g^2 modes display a heightened sensitivity to the increased surface area along the armchair direction as opposed to the B_{2g} mode. Although not as significant, an increase in activity for all the high-frequency Raman modes with a planar growth along zigzag direction can be observed. The novelty of the characterization of Raman spectra for these PQDs lay in the unraveling of the distinctly different energy shifts observed for the A_g^1 and A_g^2 modes with increasing PQD size along the two directions. The red shifting behavior observed for these modes with increasing system size along the armchair direction is attributed to the dominance of the mass coupling over improved bonding, while the blue shifts observed with an increase of system size along the zigzag direction is attributed to the dominance of improved bonding strength over mass coupling (mostly present in the A_g^2 peak). Similar trends also can be observed with the B_{2g}mode, however forming a conclusive narrative is challenging owing to the relatively smaller Raman activities coupled with the artifacts of edge groups convoluting the Raman response. Furthermore, the type of edge termination only plays a minor role in the Raman response. These effects generally arise through changes in surface area that is polarizable, leading to a change in Raman activity, or changes to the electron density distribution corresponding to a change in bonding leading to shifts in the Raman peaks. Thus, the anisotropy of these PQDs plays a pivotal role in all the optical properties described in this study. The distinct behavior can be further accentuated with the effects of quantum confinement, while

the role of the edge terminating group is often limited to minor affects arising from the perturbations to electron density of the system.

5. Supporting Information

The Supporting Information is available free of charge on the ACS Publications website at DOI: xxx.xxx.

Top view of $P_{28}X_{14}$ and $P_{110}X_{30}$ PQDs where X represents edge functional groups; Geometric, electronic, and optical properties of functionalized PQDs; CAM-B3LYP generated absorption spectra of hydrogen functionalized PQDs; Comparison of B3LYP and CAM-B3LYP generated absorption spectra for low lying excitations of hydrogen functionalized PQDs; DOS and PDOS of hydrogen functionalized PQDs; HOMO, LUMO energy diagrams for S_0 and S_1 states of hydrogen functionalized PQDs; A_g^1 and A_g^2 Raman active vibrational modes for $P_{28}H_{14}$ and $P_{110}H_{30}$ PQDs; Analysis of A_g^1 and A_g^2 Raman modes for hydrogen terminated PQDs; Raman spectra for all PQDS

6. Acknowledgments

This material is based upon work supported by the National Science Foundation under Grant No. 2147956. The authors acknowledge Baylor University High Performance and Research Computing Services for their support of the research reported in this paper.

7. References

(1) Novoselov, K. S.; Geim, A. K.; Morozov, S. V.; Jiang, D.; Zhang, Y.; Dubonos, S. V.; Grigorieva, I. V.; Firsov, A. A. Electric Field Effect in Atomically Thin Carbon Films. *Science* **2004**, *306*, 666-669.

(2) Novoselov, K. S.; Jiang, D.; Schedin, F.; Booth, T. J.; Khotkevich, V. V.; Morozov, S. V.; Geim, A. K. Two-dimensional atomic crystals. *Proc. Natl. Acad. Sci. U. S. A.* **2005**, *102*, 10451-10453.

(3) Liu, H.; Neal, A. T.; Zhu, Z.; Luo, Z.; Xu, X.; Tománek, D.; Ye, P. D. Phosphorene: An Unexplored 2D Semiconductor with a High Hole Mobility. *ACS Nano* **2014**, *8*, 4033-4041.

(4) Li, L.; Yu, Y.; Ye, G. J.; Ge, Q.; Ou, X.; Wu, H.; Feng, D.; Chen, X. H.; Zhang, Y. Black phosphorus field-effect transistors. *Nat. Nanotechnol.* **2014**, *9*, 372-377.

(5) Kou, L.; Chen, C.; Smith, S. C. Phosphorene: Fabrication, Properties, and Applications. *J. Phys. Chem. Lett.* **2015**, *6*, 2794-2805.

(6) Xia, F.; Wang, H.; Jia, Y. Rediscovering Black Phosphorus as an Anisotropic Layered Material for Optoelectronics and Electronics. *Nat. Commun.* **2014**, *5*, 4458.

(7) Huang, M.; Wang, M.; Chen, C.; Ma, Z.; Li, X.; Han, J.; Wu, Y. Broadband Black-Phosphorus Photodetectors with High Responsivity. *Adv. Mater.* **2016**, *28*, 3481-3485.

(8) Kou, L.; Frauenheim, T.; Chen, C. Phosphorene as a Superior Gas Sensor: Selective Adsorption and Distinct I–V Response. *J. Phys. Chem. Lett.* **2014**, *5*, 2675-2681.

(9) Donarelli, M.; Ottaviano, L.; Giancaterini, L.; Fioravanti, G.; Perrozzi, F.; Cantalini, C. Exfoliated Black Phosphorus Gas Sensing Properties at Room Temperature. *2D Mater* **2016**, *3*, 025002.

(10) Ray, S. J. First-Principles Study of MoS_2, Phosphorene and Graphene based Single Electron Transistor for Gas Sensing Applications. *Sens. Actuators B Chem.* **2016**, *222*, 492-498.

(11) Zhao, S.; Kang, W.; Xue, J. The Potential Application of Phosphorene as an Anode Material in Li-ion Batteries. *J. Mater. Chem. A* **2014**, *2*, 19046-19052.

(12) Sun, J.; Zheng, G.; Lee, H.-W.; Liu, N.; Wang, H.; Yao, H.; Yang, W.; Cui, Y. Formation of Stable Phosphorus–Carbon Bond for Enhanced Performance in Black Phosphorus Nanoparticle–Graphite Composite Battery Anodes. *Nano Lett.* **2014**, *14*, 4573-4580.

(13) Slack, G. A. Thermal Conductivity of Elements with Complex Lattices: B, P, S. *Phys. Rev.* **1965**, *139*, A507-A515.

(14) Fei, R.; Faghaninia, A.; Soklaski, R.; Yan, J.-A.; Lo, C.; Yang, L. Enhanced Thermoelectric Efficiency via Orthogonal Electrical and Thermal Conductances in Phosphorene. *Nano Lett.* **2014**, *14*, 6393-6399.

(15) Jiang, J.-W. Thermal Conduction in Single-Layer Black Phosphorus: Highly Anisotropic? *Nanotechnology* **2015**, *26*, 055701.

(16) Batmunkh, M.; Bat-Erdene, M.; Shapter, J. G. Phosphorene and Phosphorene-Based Materials – Prospects for Future Applications. *Adv. Mater.* **2016**, *28*, 8586-8617.

(17) Koley, S.; Basu, S. Intercalated Phosphorene for Improved Spintronic Applications. *IEEE Transactions on Magnetics* **2021**, *57*, 1-7.

(18) Babar, R.; Kabir, M. Transition Metal and Vacancy Defect Complexes in Phosphorene: A Spintronic Perspective. *J. Phys. Chem. C* **2016**, *120*, 14991-15000.

(19) Tatullo, M.; Genovese, F.; Aiello, E.; Amantea, M.; Makeeva, I.; Zavan, B.; Rengo, S.; Fortunato, L. Phosphorene Is the New Graphene in Biomedical Applications. *Materials* **2019**, *12*, 2301.

(20) Luo, M.; Fan, T.; Zhou, Y.; Zhang, H.; Mei, L. 2D Black Phosphorus–Based Biomedical Applications. *Adv. Funct. Mater.* **2019**, *29*, 1808306.

(21) Choi, J. R.; Yong, K. W.; Choi, J. Y.; Nilghaz, A.; Lin, Y.; Xu, J.; Lu, X. Black Phosphorus and its Biomedical Applications. *Theranostics* **2018**, *8*, 1005-1026.

(22) Lin, S.; Chui, Y.; Li, Y.; Lau, S. P. Liquid-phase exfoliation of black phosphorus and its applications. *FlatChem* **2017**, *2*, 15-37.

(23) Brent, J. R.; Savjani, N.; Lewis, E. A.; Haigh, S. J.; Lewis, D. J.; O'Brien, P. Production of Few-Layer Phosphorene by Liquid Exfoliation of Black Phosphorus. *Chem. Commun.* **2014**, *50*, 13338-13341.

(24) Hanlon, D.; Backes, C.; Doherty, E.; Cucinotta, C. S.; Berner, N. C.; Boland, C.; Lee, K.; Harvey, A.; Lynch, P.; Gholamvand, Z.; et al. Liquid exfoliation of solvent-stabilized few-layer black phosphorus for applications beyond electronics. *Nat. Commun.* **2015**, *6*, 8563.

(25) Smith, J. B.; Hagaman, D.; Ji, H.-F. Growth of 2D black phosphorus film from chemical vapor deposition. *Nanotechnology* **2016**, *27*, 215602.

(26) Khurram, M.; Sun, Z.; Zhang, Z.; Yan, Q. Chemical vapor transport growth of bulk black phosphorus single crystals. *Inorg. Chem. Front.* **2020**, *7*, 2867-2879.

(27) Xu, H.; Han, X.; Li, Z.; Liu, W.; Li, X.; Wu, J.; Guo, Z.; Liu, H. Epitaxial Growth of Few-Layer Black Phosphorene Quantum Dots on Si Substrates. *Adv. Mater. Interfaces* **2018**, *5*, 1801048.

(28) Zhang, W.; Enriquez, H.; Tong, Y.; Mayne, A. J.; Bendounan, A.; Smogunov, A.; Dappe, Y. J.; Kara, A.; Dujardin, G.; Oughaddou, H. Flat epitaxial quasi-1D phosphorene chains. *Nat. Commun.* **2021**, *12*, 5160.

(29) Jang, H.; Wood, J. D.; Ryder, C. R.; Hersam, M. C.; Cahill, D. G. Anisotropic Thermal Conductivity of Exfoliated Black Phosphorus. *Adv. Mater.* **2015**, *27*, 8017-8022.

(30) Xu, Y.; Dai, J.; Zeng, X. C. Electron-Transport Properties of Few-Layer Black Phosphorus. *J. Phys. Chem. Lett.* **2015**, *6*, 1996-2002.

(31) Rodin, A. S.; Carvalho, A.; Castro Neto, A. H. Strain-Induced Gap Modification in Black Phosphorus. *Phys. Rev. Lett.* **2014**, *112*, 176801.

(32) Wei, Q.; Peng, X. Superior Mechanical Flexibility of Phosphorene and Few-Layer Black Phosphorus. *Appl. Phys. Lett.* **2014**, *104*, 251915.

(33) Jiang, J.-W.; Park, H. S. Mechanical Properties of Single-Layer Black Phosphorus. *J. Phys. D Appl. Phys.* **2014**, *47*, 385304.

(34) Jiang, J.-W.; Park, H. S. Negative Poisson's Ratio in Single-Layer Black Phosphorus. *Nat. Commun.* **2014**, *5*, 4727.

(35) Wu, J.; Mao, N.; Xie, L.; Xu, H.; Zhang, J. Identifying the Crystalline Orientation of Black Phosphorus Using Angle-Resolved Polarized Raman Spectroscopy. *Angew. Chem. Int. Ed.* **2015**, *54*, 2366-2369.

(36) Takao, Y.; Asahina, H.; Morita, A. Electronic Structure of Black Phosphorus in Tight Binding Approach. *J. Phys. Sco. Jpn.* **1981**, *50*, 3362-3369.

(37) Asahina, H.; Shindo, K.; Morita, A. Electronic Structure of Black Phosphorus in Self-Consistent Pseudopotential Approach. *J. Phys. Sco. Jpn.* **1982**, *51*, 1193-1199.

(38) Brunetti, M. N.; Berman, O. L.; Kezerashvili, R. Y. Optical properties of anisotropic excitons in phosphorene. *Phys. Rev. B* **2019**, *100*, 155433.

(39) Tran, V.; Soklaski, R.; Liang, Y.; Yang, L. Layer-controlled band gap and anisotropic excitons in few-layer black phosphorus. *Phys. Rev. B* **2014**, *89*, 235319.

(40) Saberi-Pouya, S.; Zarenia, M.; Perali, A.; Vazifehshenas, T.; Peeters, F. M. High-temperature electron-hole superfluidity with strong anisotropic gaps in double phosphorene monolayers. *Phys. Rev. B* **2018**, *97*, 174503.

(41) Berman, O. L.; Gumbs, G.; Kezerashvili, R. Y. Bose-Einstein condensation and superfluidity of dipolar excitons in a phosphorene double layer. *Phys. Rev. B* **2017**, *96*, 014505.

(42) Li, P.; Appelbaum, I. Electrons and holes in phosphorene. *Phys. Rev. B* **2014**, *90*, 115439.

(43) Tran, V.; Yang, L. Scaling laws for the band gap and optical response of phosphorene nanoribbons. *Phys. Rev. B* **2014**, *89*, 245407.

(44) Bhattacharyya, P.; Chaudhari, R.; Alaal, N.; Rana, T.; Shukla, A. Influence of Edge Functionalization on Electronic and Optical Properties of Armchair Phosphorene Nanoribbons: A First-Principles Study. *Electron. Struct.* **2020**, *2*, 025001.

(45) Li, L. L.; Moldovan, D.; Xu, W.; Peeters, F. M. Electric- and magnetic-field dependence of the electronic and optical properties of phosphorene quantum dots. *Nanotechnology* **2017**, *28*, 085702.

(46) Saroka, V. A.; Lukyanchuk, I.; Portnoi, M. E.; Abdelsalam, H. Electro-optical properties of phosphorene quantum dots. *Phys. Rev. B* **2017**, *96*, 085436.

(47) Jiang, Z. T.; Liang, F. X.; Lv, Z. T.; Ren, Y. H.; Han, Q. Z. Symmetry effect on the mechanism of the optical absorption of phosphorene quantum dots. *Physica E: Low-dimensional Systems and Nanostructures* **2019**, *107*, 137-141.

(48) Niu, X.; Li, Y.; Shu, H.; Wang, J. Anomalous Size Dependence of Optical Properties in Black Phosphorus Quantum Dots. *J. Phys. Chem. Lett.* **2016**, *7*, 370-375.

(49) Abdelsalam, H.; Zhang, Q. F. Properties and applications of quantum dots derived from two-dimensional materials. *Advances in Physics: X* **2022**, *7*, 2048966.

(50) Han, S.-T.; Hu, L.; Wang, X.; Zhou, Y.; Zeng, Y.-J.; Ruan, S.; Pan, C.; Peng, Z. Black Phosphorus Quantum Dots with Tunable Memory Properties and Multilevel Resistive Switching Characteristics. *Adv. Sci.* **2017**, *4*, 1600435.

(51) Prasannachandran, R.; Vineesh, T. V.; Anil, A.; Krishna, B. M.; Shaijumon, M. M. Functionalized Phosphorene Quantum Dots as Efficient Electrocatalyst for Oxygen Evolution Reaction. *ACS Nano* **2018**, *12*, 11511-11519.

(52) Li, Y.; Liu, Z.; Hou, Y.; Yang, G.; Fei, X.; Zhao, H.; Guo, Y.; Su, C.; Wang, Z.; Zhong, H.; et al. Multifunctional Nanoplatform Based on Black Phosphorus Quantum Dots for Bioimaging and Photodynamic/Photothermal Synergistic Cancer Therapy. *ACS Appl. Mater. Interfaces* **2017**, *9*, 25098-25106.

(53) Bondi, A. van der Waals Volumes and Radii. *J. Phys. Chem.* **1964**, *68*, 441-451.

(54) Lu, T.; Chen, F. Multiwfn: A multifunctional wavefunction analyzer. *J. Comput. Chem.* **2012**, *33*, 580-592.

(55) De Alwis, W. M. U. G.; Weerawardene, K. L. D. M.; Ellington, T. L.; Shuford, K. L. Electronic Structure Modification of Rectangular Phosphorene Quantum Dots Via Edge Passivation. *J. Phys. Chem. C* **2021**, *125*, 5029-5036.

(56) Becke, A. D. Density-Functional Thermochemistry. III. The Role of Exact Exchange. *J. Chem. Phys.* **1993**, *98*, 5648-5652.

(57) Stephens, P. J.; Devlin, F. J.; Chabalowski, C. F.; Frisch, M. J. Ab Initio Calculation of Vibrational Absorption and Circular Dichroism Spectra Using Density Functional Force Fields. *J. Phys. Chem.* **1994**, *98*, 11623-11627.

(58) Lee, C.; Yang, W.; Parr, R. G. Development of the Colle-Salvetti correlation-energy formula into a functional of the electron density. *Phys. Rev. B* **1988**, *37*, 785-789.

(59) Casida, M. E.; Jamorski, C.; Casida, K. C.; Salahub, D. R. Molecular excitation energies to high-lying bound states from time-dependent density-functional response theory:

Characterization and correction of the time-dependent local density approximation ionization threshold. *J. Chem. Phys.* **1998**, *108*, 4439-4449.

(60) Stratmann, R. E.; Scuseria, G. E.; Frisch, M. J. An efficient implementation of time-dependent density-functional theory for the calculation of excitation energies of large molecules. *J. Chem. Phys.* **1998**, *109*, 8218-8224.

(61) Van Caillie, C.; Amos, R. D. Geometric derivatives of excitation energies using SCF and DFT. *Chemical Physics Letters* **1999**, *308*, 249-255.

(62) Bauernschmitt, R.; Ahlrichs, R. Treatment of electronic excitations within the adiabatic approximation of time dependent density functional theory. *Chemical Physics Letters* **1996**, *256*, 454-464.

(63) Schira, R.; Rabilloud, F. Localized Surface Plasmon Resonance in Free Silver Nanoclusters Agn, n = 20–147. *J. Phys. Chem. C* **2019**, *123*, 6205-6212.

(64) Temelso, B.; Mabey, J. M.; Kubota, T.; Appiah-Padi, N.; Shields, G. C. ArbAlign: A Tool for Optimal Alignment of Arbitrarily Ordered Isomers Using the Kuhn–Munkres Algorithm. *J. Chem. Inf. Model.* **2017**, *57*, 1045-1054.

(65) Kuhn, H. W. The Hungarian method for the assignment problem. *Naval Research Logistics Quarterly* **1955**, *2*, 83-97.

(66) Munkres, J. Algorithms for the Assignment and Transportation Problems. *J. Soc. Indust. Appl. Math.* **1957**, *5*, 32-38.

(67) Frisch, M. J.; Trucks, G. W.; Schlegel, H. B.; Scuseria, G. E.; Robb, M. A.; Cheeseman, J. R.; Scalmani, G.; Barone, V.; Petersson, G. A.; Nakatsuji, H.; , et al., *Gaussian 16 Rev. C.01*, Wallingford, CT, 2016.

(68) Stone, J. An Efficient Library for Parallel Ray Tracing and Animation. Masters Theses, Missouri University of Science and Technology, **1998**.

(69) Humphrey, W.; Dalke, A.; Schulten, K. VMD: Visual Molecular Dynamics. *J. Mol. Graph.* **1996**, *14*, 33-38.

(70) Yanai, T.; Tew, D. P.; Handy, N. C. A new hybrid exchange–correlation functional using the Coulomb-attenuating method (CAM-B3LYP). *Chemical Physics Letters* **2004**, *393*, 51-57.

(71) Englman, R.; Jortner, J. The energy gap law for radiationless transitions in large molecules. *Molecular Physics* **1970**, *18*, 145-164.

(72) Jang, S. J. A simple generalization of the energy gap law for nonradiative processes. *The Journal of Chemical Physics* **2021**, *155*, 164106.

(73) Mori, K.; Goumans, T. P. M.; van Lenthe, E.; Wang, F. Predicting phosphorescent lifetimes and zero-field splitting of organometallic complexes with time-dependent density functional theory including spin–orbit coupling. *Phys. Chem. Chem. Phys.* **2014**, *16*, 14523-14530.

(74) Weerawardene, K. L. D. M.; Aikens, C. M. Origin of Photoluminescence of Ag25(SR)18– Nanoparticles: Ligand and Doping Effect. *J. Phys. Chem. C* **2018**, *122*, 2440-2447.

(75) Guidez, E. B.; Aikens, C. M. Time-Dependent Density Functional Theory Study of the Luminescence Properties of Gold Phosphine Thiolate Complexes. *J. Phys. Chem. A* **2015**, *119*, 3337-3347.

(76) Ling, X.; Liang, L.; Huang, S.; Puretzky, A. A.; Geohegan, D. B.; Sumpter, B. G.; Kong, J.; Meunier, V.; Dresselhaus, M. S. Low-Frequency Interlayer Breathing Modes in Few-Layer Black Phosphorus. *Nano Lett.* **2015**, *15*, 4080-4088.

(77) Sugai, S.; Shirotani, I. Raman and infrared reflection spectroscopy in black phosphorus. *Solid State Communications* **1985**, *53*, 753-755.

(78) Favron, A.; Gaufrès, E.; Fossard, F.; Phaneuf-L'Heureux, A.-L.; Tang, N. Y. W.; Lévesque, P. L.; Loiseau, A.; Leonelli, R.; Francoeur, S.; Martel, R. Photooxidation and quantum confinement effects in exfoliated black phosphorus. *Nat Mater.* **2015**, *14*, 826-832.

(79) Tokár, K.; Brndiar, J.; Štich, I. Raman Activity of Multilayer Phosphorene under Strain. *ACS Omega* **2019**, *4*, 22418-22425.

(80) Feng, Y.; Zhou, J.; Du, Y.; Miao, F.; Duan, C.-G.; Wang, B.; Wan, X. Raman spectra of few-layer phosphorene studied from first-principles calculations. *J. Phys.: Condens. Matter* **2015**, *27*, 185302.

TOC Graphic